

A moving grid finite element method applied to a model biological pattern generator

Anotida Madzvamuse

*Oxford University Computing Laboratory, Wolfson Building,
Parks Road, Oxford OX1 3QD, UK*

Andrew J. Wathen

*Oxford University Computing Laboratory, Wolfson Building,
Parks Road, Oxford OX1 3QD, UK*

Philip K. Maini

*Centre for Mathematical Biology, Mathematical Institute, University of Oxford,
24–29 St Giles', Oxford OX1 3LB, UK*

Many problems in biology involve growth. In numerical simulations it can therefore be very convenient to employ a moving computational grid on a continuously deforming domain. In this paper we present a novel application of the moving grid finite element method to compute solutions of reaction-diffusion systems in two-dimensional continuously deforming Euclidean domains. A numerical software package has been developed as a result of this research that is capable of solving generalised Turing models of morphogenesis.

Key words and phrases: This paper has been submitted to the Journal of Computational Physics

Oxford University Computing Laboratory
Numerical Analysis Group
Wolfson Building
Parks Road
Oxford, England OX1 3QD

November, 2002

¹This work supported by EPSRC Life Sciences Initiative grant GR/R03914

1 Introduction

Understanding how spatial pattern arises is a central but still unresolved issue in developmental biology. It is clear that genes play a crucial role in embryology but the study of genetics alone can not explain how the complex mechanical and chemical spatio-temporal signalling cues which determine cell fate are set up and regulated in the early embryo. These signals are a consequence of many nonlinear interactions and mathematical modelling and numerical computation have an important role to play in understanding and predicting the outcome of such complex interactions.

The application of mathematical modelling to problems in developmental biology has given rise to a variety of models which account for spatio-temporal patterning phenomena. In the chemical prepatterning model approach it is hypothesised that a spatially homogeneous or uniform density of cells responds to some spatially heterogeneous chemical pattern and differentiates according to some rules. Turing (1952) in his seminal paper concerning morphogenesis, suggested a novel concept of diffusion driven instability in reaction-diffusion systems. Since then, the reaction-diffusion theory of pattern formation has been widely applied to biology, ecology (Segel and Jackson, 1972), semiconductor physics (Balkarev *et al.*, 1988), material science (Krinsky, 1984), hydrodynamics (White, 1988), astrophysics (Nozakura and Ikeuchi, 1984), chemistry and economics. Typical examples of biological applications of reaction-diffusion systems are: pattern formation in hydra (Gierer and Meinhardt, 1972), animal coat markings (Murray, 1981), butterfly wing pigmentation patterns (Nijhout, 1990), skeletal patterning in limb development (see, for review, Maini and Solursh, 1991) and shell pigmentation patterns (Meinhardt, 1995). Detailed studies of these models have been carried out on spatial domains of one dimension and two dimensions with simple geometries. In nearly all these cases, the domain was considered fixed in size, however recent experimental evidence shows that domain growth may play a crucial role in pattern formation (Kondo and Asai, 1995).

From the biologically realistic assumption that growth occurs via a continuous deformation of the domain, we can solve the system numerically using the finite element method on a continuously deforming domain (Baines, 1994). The essential component underlying this method is the representation of the object function by a piecewise linear continuous function on a finite element mesh in which the nodal positions vary with time. The way in which these nodes are moved and how the solution evolves is derived in the weak form of the model system. The nodal movement can either be provided by a separate definition or by a mechanism: we will prescribe a specific definition for the motion of the domain and correspondingly define the motion of all the nodes in the grid. This is the key difference to the moving finite element method invented by Miller in 1981 (Miller and Miller, 1981). Miller does not specify the motion of the nodes, instead the nodal movement is generated automatically by minimising the residual of the differential equation. In his method mesh tangling may result whereas this can be avoided with prescribed mesh motion.

In section 2 we present the model equations considered in this paper. The moving grid finite element theory is described in section 3. Here we derive the weak form of the partial differential equation and describe the Galerkin Finite element approximation on a continuously deforming grid. Numerical experiments are presented in section 4 on regular

and irregular growing domains. Lastly in section 5 we present conclusions and discuss the implications of the novel application of the moving finite element method to pattern formation and transition in biological problems. We also provide numerical software and documentation for the methods described in this paper which can be freely downloaded from (<http://web.comlab.ox.ac.uk/oucl/work/andy.wathen/software.html>).

2 Model equations

The numerical experiments in this paper will be restricted to a generalised reaction-diffusion system of two chemical species which can be written in terms of non-dimensional variables as

$$\frac{\partial \mathbf{u}}{\partial t} = \gamma \mathbf{f}(\mathbf{u}) + \mathbf{P}_3(\mathbf{u}) + \mathbf{D} \nabla^2 \mathbf{u} \quad \text{in } \Omega(t), \quad (2.1)$$

with $\Omega(t)$ representing a time-dependent domain. Here we define

$$\mathbf{u} = \begin{pmatrix} u \\ v \end{pmatrix}, \quad \mathbf{f} = \begin{pmatrix} f(u, v) \\ g(u, v) \end{pmatrix}, \quad \mathbf{P}_3 = \begin{pmatrix} p_3(u, v) \\ q_3(u, v) \end{pmatrix}, \quad \mathbf{D} = \begin{pmatrix} 1 & 0 \\ 0 & d \end{pmatrix}, \quad \mathbf{x} = (x(t), y(t)) \quad (2.2)$$

where u, v are the two chemical concentrations under investigation, f, g, p_3, q_3 are reaction kinetics, and \mathbf{D} is the diffusion matrix. In a number of important applications the parameter γ and d are the most important and this is why they are explicitly included in (2.1).

Initial conditions are given by $\mathbf{u}(\mathbf{x}, 0) = \mathbf{u}_0(\mathbf{x})$ where $\mathbf{u}_0(\mathbf{x})$ is a prescribed non-negative continuous bounded function. Boundary conditions can be of Dirichlet type (u and/or v given on the boundary) or of (homogeneous) Neumann type which describe zero-flux of u (or v) out of the boundary. Initial conditions are defined as small random perturbations about the uniform homogeneous steady state, if it exists (i.e. a state $u = \text{constant}$, $v = \text{constant}$ satisfying the boundary conditions and equations (2.1)).

Below we consider three special cases where $\gamma \neq 0$ and $p_3(u, v) = 0 = q_3(u, v)$. In each case we give a brief description of each model and its physical interpretation.

2.1 Gierer-Meinhardt reaction kinetics

This is a phenomenological model suggested by Gierer and Meinhardt (1972) whereby reaction kinetics are chosen in such a way that one of the chemicals (termed activator) activates the production of the other chemical (the inhibitor) which, in turn, inhibits the production of the activator. The non-dimensionalised reaction-diffusion system is given by

$$\frac{\partial u}{\partial t} = \gamma \left(a - b u + \frac{u^2}{v(1 + k u^2)} \right) + \nabla^2 u, \quad (2.3)$$

$$\frac{\partial v}{\partial t} = \gamma (u^2 - v) + d \nabla^2 v \quad (2.4)$$

where $u(x, y, t)$ is the concentration of the activator, $v(x, y, t)$ is the concentration of the inhibitor, t is time and $\nabla^2 = \frac{\partial^2}{\partial x^2} + \frac{\partial^2}{\partial y^2}$ is the 2-dimensional Laplacian. a, b, d and γ are all nondimensionalised positive parameters and k is a measure of the saturation concentration (see, for example, Murray, 1993). The biological interpretation of the reaction kinetics in (2.3) is that u is produced at a constant rate γa and is degraded linearly at rate γb . The $\gamma \frac{u^2}{v(1+ku^2)}$ term implies autocatalysis in u with saturation at high concentration values of u , and inhibition of u through the production of v . In equation (2.4), v is activated (produced) by u and degraded linearly.

2.2 Thomas reaction kinetics

This model is based on a specific substrate-inhibition reaction involving the substrates oxygen ($v(x, y, t)$) and uric acid ($u(x, y, t)$) which react in the presence of the enzyme uricase. The reaction kinetics, derived by fitting the kinetics to experimental data (Thomas, 1975), can be written in nondimensional form as

$$\frac{\partial u}{\partial t} = \gamma (a - u - h(u, v)) + \nabla^2 u, \quad (2.5)$$

$$\frac{\partial v}{\partial t} = \gamma (\alpha b - \alpha v - h(u, v)) + d \nabla^2 v \quad (2.6)$$

with $h(u, v) = \frac{\rho uv}{1+u+Ku^2}$. Here $a, b, d, \gamma, \alpha, \rho$ and K are positive parameters. The term $h(u, v)$ indicates the rate at which u and v are used up, in particular $h(u, v)$ exhibits what is known as substrate-inhibition, that is, for small u , $h(u, v)$ increases with u , while it decreases with large u .

2.3 Schnakenberg reaction kinetics

This is one of the simplest reaction-diffusion models. It is derived from a series of hypothetical tri-molecular autocatalytic reactions proposed by Schnakenberg (1979). In nondimensional form the system is written as

$$\frac{\partial u}{\partial t} = \gamma (a - u + u^2 v) + \nabla^2 u, \quad (2.7)$$

$$\frac{\partial v}{\partial t} = \gamma (b - u^2 v) + d \nabla^2 v \quad (2.8)$$

where a, b, d and γ are positive parameters. The biological interpretation follows as above, with the term $u^2 v$ representing nonlinear activation of u and nonlinear consumption for v .

2.4 Other reaction kinetics

If $\gamma = 0$, $p_3(u, v) \neq 0$ and $q_3(u, v) \neq 0$ then the reaction-diffusion system (2.1) becomes

$$\frac{\partial \mathbf{u}}{\partial t} = \mathbf{P}_3(\mathbf{u}) + \mathbf{D} \nabla^2 \mathbf{u} \quad (2.9)$$

where

$$\begin{aligned} p_3(u, v) &= a_0 + a_1 u + a_2 v + a_3 u^2 + a_4 u v + a_5 v^2 + a_6 u^3 + a_7 u^2 v + a_8 u v^2 + a_9 v^3, \\ q_3(u, v) &= b_0 + b_1 u + b_2 v + b_3 u^2 + b_4 u v + b_5 v^2 + b_6 u^3 + b_7 u^2 v + b_8 u v^2 + b_9 v^3 \end{aligned}$$

are general bivariate cubic polynomials with a_i and b_i ($i = 0, \dots, 9$) being constant coefficients. Note that the Schnakenberg reaction kinetics is a special case of (2.9). Another special case is the Gray-Scott (1983, 1984) model. More special cases can be found in the papers by Barrio *et al.*, 1999, 2002 and Aragon *et al.*, 1998, 2002.

2.5 Parameter values

The parameter values in the reaction terms are those that give a constant uniform steady state in the absence of diffusion. In our investigations, these are taken from literature (Murray, 1993). However, the values of γ and the diffusion coefficient d are determined from the conditions that give rise to Turing instability. Turing instability or diffusion-driven instability occurs when a uniform steady state, linearly stable in the absence of diffusion, goes unstable in the presence of diffusion. The process of determining these parameter values is known as linear stability analysis (Appendix A). On regular two-dimensional shapes, standard linear stability analysis yields general solutions which are linear combinations of products of sine or cosine functions with mode (m, n) . These are the eigenfunctions of the Laplacian with homogeneous Neumann boundary conditions. Comparisons will be made between the numerically computed inhomogeneous steady state solutions and their corresponding eigenfunctions on regular domains.

3 The moving grid finite element method

Let \mathbf{U} be the finite element approximation to \mathbf{u} defined as

$$\mathbf{U}(\mathbf{x}, t) = \sum_{i=0}^{N+1} \mathbf{U}_i(t) \phi_i(\mathbf{x}, \mathbf{a}(t)) \quad (3.1)$$

where $\mathbf{x} \in \mathbb{R}^m$ indicates the spatial coordinates and $\mathbf{a}(t)$ represents the grid in time, that is the vector of nodal positions at time t . This grid is given by $\mathbf{a}(t) = (a_0(t), a_1(t), \dots, a_{N+1}(t))^T$ where $\mathbf{a}_i(t) = (x_i(t), y_i(t))^T$ is the position vector of the i th node. Here, $\phi_i(\mathbf{x}, \mathbf{a}(t))$ is the piecewise linear hat function, which is defined to be the unique piecewise linear and continuous function on the grid such that $\phi_i(\mathbf{a}_j, \mathbf{a}(t)) = \delta_{i,j}$. We calculate the time derivative of the finite element approximation \mathbf{U} as given by

$$\frac{\partial \mathbf{U}}{\partial t} = \sum_{i=0}^{N+1} \frac{\partial}{\partial t} (\mathbf{U}_i(t) \phi_i(\mathbf{x}, \mathbf{a}(t))). \quad (3.2)$$

Applying the product rule we have

$$\frac{\partial \mathbf{U}}{\partial t} = \sum_{i=0}^{N+1} \left[\frac{d\mathbf{U}_i}{dt} \phi_i + \mathbf{U}_i \frac{\partial \phi_i}{\partial t} \right]. \quad (3.3)$$

Now applying the chain rule to the last term we obtain (Jimack and Wathen, 1991)

$$\frac{\partial \mathbf{U}}{\partial t} = \sum_{i=0}^{N+1} \frac{d\mathbf{U}_i}{dt} \phi_i + \sum_{i=0}^{N+1} \beta_i^T \dot{\mathbf{a}}_i(t) \quad (3.4)$$

where $\beta_i = \frac{\partial \mathbf{U}}{\partial \mathbf{a}_i}$. Baines and Wathen (1988) proved that $\beta_i = \frac{\partial \mathbf{U}}{\partial a_i} = -\phi_i \frac{\partial \mathbf{U}}{\partial \mathbf{x}}$ in multi-dimensions. In particular $\beta_i = -\phi_i \mathbf{U}_x$ with $\dot{\mathbf{a}}_i = \dot{x}_i$ in one dimension and $\dot{\mathbf{a}}_i = (\dot{x}_i, \dot{y}_i)^T$ in two dimensions. Therefore the time derivative of \mathbf{U} is given by

$$\frac{\partial \mathbf{U}}{\partial t} = \sum_{i=0}^{N+1} \left[\dot{\mathbf{U}}_i - \dot{x}_i \mathbf{U}_x \right] \phi_i(\mathbf{x}, \mathbf{a}(t)) \quad (3.5)$$

in one dimension and in two dimensions by

$$\frac{\partial \mathbf{U}}{\partial t} = \sum_{i=0}^{N+1} \left[\dot{\mathbf{U}}_i - (\dot{x}_i \mathbf{U}_x + \dot{y}_i \mathbf{U}_y) \right] \phi_i(\mathbf{x}, \mathbf{a}(t)). \quad (3.6)$$

The effect of the growing domain is to add extra terms to the finite element formulation as illustrated in the general case (3.4) and in particular for (3.5) and (3.6) in the one- and two-dimensional cases respectively. The key difference to the moving finite element method invented by Miller (1981) is that we prescribe a specific definition for the nodal movement $\dot{\mathbf{a}}_i$. We assume that nodal movement can be determined or prescribed, for example, growth rates derived from biological observations.

3.1 Spatial discretisation: Finite element method

In order to discretise the model equations (2.1) in space, one has to divide the domain under consideration into a series of non-overlapping sub-domains or elements. The problem is then approximated within each of these elements, and the corresponding element contributions are summed to create a global system of equations.

The discretisation of the geometry is carried out by using triangular elements with a piecewise linear approximation to the solution. We impose the conditions that the elements must cover the entire domain without leaving gaps (except perhaps at the boundary), that is, any pair of elements intersect along a complete edge, at a vertex or not at all. If we cover a region $\Omega(t)$ with triangular elements, then each element can be mapped onto a standard fixed regular triangle at time t . This simplifies the required integration over each triangular element.

Let \mathbf{U} be defined as in (3.1) such that the family of the functions ϕ_i are linearly independent. Although we consider a finite-dimensional space in practice for the basis functions ϕ_i , we assume that as N tends to infinity, convergence is possible since the limit space is dense in $H^1(\Omega(t))$. Over each triangular element, (e) say, \mathbf{U} can be expressed as $\mathbf{U}^{(e)}(x, y) = c_1(t) + c_2(t)x(t) + c_3(t)y(t)$. We require that $\mathbf{U}^{(e)}(x_i, y_i, t) = \mathbf{U}_i^{(e)}$, ($i = 1, 2, 3$). Therefore

$$\mathbf{U}_1(t) = c_1(t) + c_2(t)x_1(t) + c_3(t)y_1(t), \quad (3.7)$$

$$\mathbf{U}_2(t) = c_1(t) + c_2(t)x_2(t) + c_3(t)y_2(t), \quad (3.8)$$

$$\mathbf{U}_3(t) = c_1(t) + c_2(t)x_3(t) + c_3(t)y_3(t). \quad (3.9)$$

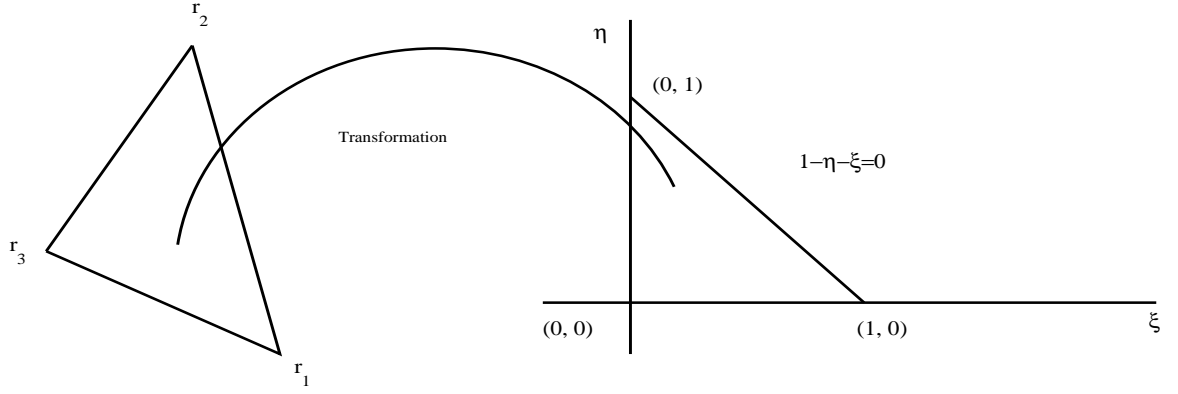


Figure 1: Transformation of a general triangle into a canonical triangle and local coordinates.

Solving this system of algebraic equations results in

$$c_1(t) = \frac{1}{2 A_{123}(t)} (\alpha_1 \mathbf{U}_1(t) + \alpha_2 \mathbf{U}_2(t) + \alpha_3 \mathbf{U}_3(t)), \quad (3.10)$$

$$c_2(t) = \frac{1}{2 A_{123}(t)} (\beta_1 \mathbf{U}_1(t) + \beta_2 \mathbf{U}_2(t) + \beta_3 \mathbf{U}_3(t)), \quad (3.11)$$

$$c_3(t) = \frac{1}{2 A_{123}(t)} (\tau_1 \mathbf{U}_1(t) + \tau_2 \mathbf{U}_2(t) + \tau_3 \mathbf{U}_3(t)), \quad (3.12)$$

where $A_{123}(t)$ is the area of the triangle and $\alpha_i = x_j(t) y_k(t) - x_k(t) y_j(t)$, $\beta_i = y_j(t) - y_k(t)$, and $\tau_i = -(x_j(t) - x_k(t))$ where $i, j, k = 1, 2, 3$. Substituting (3.10)–(3.12) into $\mathbf{U}^{(e)}$ results in $\mathbf{U}^{(e)}(x, y, t) = \sum_{j=1}^3 \mathbf{U}_j(t) \phi_j(x(t), y(t))$ where

$$\phi_1 = \frac{1}{2 A_{123}(t)} (\alpha_1 + \beta_1 x(t) + \tau_1 y(t)), \quad (3.13)$$

$$\phi_2 = \frac{1}{2 A_{123}(t)} (\alpha_2 + \beta_2 x(t) + \tau_2 y(t)), \quad (3.14)$$

$$\phi_3 = \frac{1}{2 A_{123}(t)} (\alpha_3 + \beta_3 x(t) + \tau_3 y(t)). \quad (3.15)$$

Let each triangle be mapped onto a unit right-angled triangle by an affine transformation from global Cartesian coordinates $\mathbf{r} = (x(t), y(t))$ to local coordinates (ξ, η) (see Figure 1) by linear hat functions defined by

$$\mathbf{r} = (x(\xi, \eta, t), y(\xi, \eta, t)) = (1 - \xi - \eta) (x_1(t), y_1(t)) + \xi (x_2(t), y_2(t)) + \eta (x_3(t), y_3(t)) \quad (3.16)$$

or equivalently,

$$x(\xi, \eta, t) = (1 - \xi - \eta) x_1(t) + \xi x_2(t) + \eta x_3(t), \quad (3.17)$$

$$y(\xi, \eta, t) = (1 - \xi - \eta) y_1(t) + \xi y_2(t) + \eta y_3(t). \quad (3.18)$$

Here we define $\mathbf{r}_1 = (x_1, y_1)$, $\mathbf{r}_2 = (x_2, y_2)$, and $\mathbf{r}_3 = (x_3, y_3)$. Substituting $\alpha_i, \beta_i, \tau_i$, (3.17) and (3.18) into (3.13)–(3.15) results in

$$\phi_1(\xi, \eta) = 1 - \xi - \eta, \quad (3.19)$$

$$\phi_2(\xi, \eta) = \xi, \quad (3.20)$$

$$\phi_3(\xi, \eta) = \eta. \quad (3.21)$$

The set $\{\phi_1, \phi_2, \phi_3\}$ is called a local (or nodal) basis for the set of linear functions. Therefore over each element (e), \mathbf{U} reduces to

$$\mathbf{U}^{(e)}(x(\xi, \eta, t), y(\xi, \eta, t), t) = \mathbf{U}^{(e)}(\xi, \eta, t) = \sum_{j=1}^3 \mathbf{U}_j(t) \phi_j(\xi, \eta). \quad (3.22)$$

Under (3.17) and (3.18) the global linear basis functions (3.13)–(3.15) have been transformed from the global (x, y) coordinates over each triangle to local basis linear functions (3.19)–(3.21) in local (ξ, η) coordinates. The Jacobian of this transformation is given by

$$\mathbf{J} = \begin{pmatrix} x_2(t) - x_1(t) & y_2(t) - y_1(t) \\ x_3(t) - x_1(t) & y_3(t) - y_1(t) \end{pmatrix}$$

which is constant over each element and has determinant

$$|\mathbf{J}| = \det \begin{pmatrix} x_1(t) & y_1(t) & 1 \\ x_2(t) & y_2(t) & 1 \\ x_3(t) & y_3(t) & 1 \end{pmatrix} = 2 A_{123}(t) \quad (3.23)$$

where as before $A_{123}(t)$ is the area of the global triangle in the (x, y) coordinates at time t . We now calculate the partial derivatives of \mathbf{U} . For example,

$$\begin{pmatrix} \mathbf{U}_\xi^{(e)} \\ \mathbf{U}_\eta^{(e)} \end{pmatrix} = \begin{pmatrix} x_2(t) - x_1(t) & y_2(t) - y_1(t) \\ x_3(t) - x_1(t) & y_3(t) - y_1(t) \end{pmatrix} \begin{pmatrix} \mathbf{U}_x^{(e)} \\ \mathbf{U}_y^{(e)} \end{pmatrix} \quad (3.24)$$

and inverting (3.24) we obtain

$$\begin{pmatrix} \mathbf{U}_x^{(e)} \\ \mathbf{U}_y^{(e)} \end{pmatrix} = \frac{1}{|\mathbf{J}|} \begin{pmatrix} y_3(t) - y_1(t) & -(y_2(t) - y_1(t)) \\ -(x_3(t) - x_1(t)) & x_2(t) - x_1(t) \end{pmatrix} \begin{pmatrix} \mathbf{U}_\xi^{(e)} \\ \mathbf{U}_\eta^{(e)} \end{pmatrix}. \quad (3.25)$$

On the other hand, from expression (3.22)

$$\mathbf{U}_\xi^{(e)} = \mathbf{U}_2^{(e)}(t) - \mathbf{U}_1^{(e)}(t) \quad \text{and} \quad \mathbf{U}_\eta^{(e)} = \mathbf{U}_3^{(e)}(t) - \mathbf{U}_1^{(e)}(t). \quad (3.26)$$

Therefore

$$\begin{aligned} \mathbf{U}_x^{(e)} &= \frac{1}{|\mathbf{J}|} \left((y_3(t) - y_1(t)) (\mathbf{U}_2^{(e)} - \mathbf{U}_1^{(e)}) - (y_2(t) - y_1(t)) (\mathbf{U}_3^{(e)} - \mathbf{U}_1^{(e)}) \right) \\ &= \frac{1}{|\mathbf{J}|} \left((y_2(t) - y_3(t)) \mathbf{U}_1^{(e)} + (y_3(t) - y_1(t)) \mathbf{U}_2^{(e)} + (y_1(t) - y_2(t)) \mathbf{U}_3^{(e)} \right) \end{aligned} \quad (3.27)$$

and similarly

$$\mathbf{U}_y^{(e)} = \frac{1}{|\mathbf{J}|} \left((x_3(t) - x_2(t)) \mathbf{U}_1^{(e)} + (x_1(t) - x_3(t)) \mathbf{U}_2^{(e)} + (x_2(t) - x_1(t)) \mathbf{U}_3^{(e)} \right). \quad (3.28)$$

Although we have illustrated the finite element method with piecewise linear basis functions, quadratic or higher orders forms that are more accurate could be used, though throughout we use linear basis functions as these are sufficient for our studies.

3.2 The Galerkin method

A function $\mathbf{u}(\mathbf{x})$, ($\mathbf{x} \in \mathbb{R}^2$) which is a solution to (2.1) that is C^2 in $\Omega(t)$, and is C^0 or C^1 on $\partial\Omega(t)$ (depending on whether the boundary conditions are Dirichlet or Neumann/Robin type) is called a classical solution. Multiplying (2.1) by $w \in H^1(\Omega(t))$ we have the following problem:

Find $\mathbf{u} \in H^1(\Omega(t))$ such that $(\mathbf{u}_t, w) = (\gamma \mathbf{f} + \mathbf{P}_3, w) + \mathbf{D}(\nabla^2 \mathbf{u}, w)$, for all $w \in H^1(\Omega(t))$

where

$$(\mathbf{u}, w) = \left(\int_{\Omega(t)} u w d\mathbf{x} \quad \int_{\Omega(t)} v w d\mathbf{x} \right)^T \quad (3.29)$$

is the L_2 -inner product. Here we defined the Hilbert spaces (Adams, 1975; Johnson, 1987; Brenner and Scott, 1994) by

$$L_2(\Omega(t)) = \left\{ w, w \text{ is defined on } \Omega(t) \text{ such that } \int_{\Omega(t)} |w|^2 d\mathbf{x} < \infty \right\}, \quad (3.30)$$

$$H^1(\Omega(t)) = \left\{ w \in L_2(\Omega(t)) \mid \frac{\partial w}{\partial \mathbf{x}_i} \in L_2(\Omega(t)), i = 0, \dots, N+1 \right\}. \quad (3.31)$$

Applying the Greens Theorem and assuming that homogeneous Neumann boundary conditions are used, the weak form of the PDE system leads to the problem:

Find $\mathbf{u} \in V^h$ such that $(\mathbf{u}_t, w) = (\gamma \mathbf{f} + \mathbf{P}_3, w) + \mathbf{D} a(\mathbf{u}, w)$, for all $w \in V^h \subset H^1(\Omega(t))$

where $a(\mathbf{u}, w) = - \int_{\Omega(t)} \nabla \mathbf{u} \cdot \nabla w d\mathbf{x}$. We substitute \mathbf{u} with the finite element approximation \mathbf{U} . The Galerkin form then satisfies

$$(\mathbf{U}_t, W) = (\gamma \mathbf{f} + \mathbf{P}_3, W) + \mathbf{D} a(\mathbf{U}, W), \text{ for all } W \in V^h \subset H^1(\Omega(t)).$$

Since the W_i are coefficients of the test function, the Galerkin form also satisfies

$$(\mathbf{U}_t, \varphi_i) = (\gamma \mathbf{f} + \mathbf{P}_3, \varphi_i) + \mathbf{D} a(\mathbf{U}, \varphi_i), \quad (3.32)$$

$$\frac{d\mathbf{U}_j}{dt}(\varphi_j, \varphi_i) - (\dot{x}_j \mathbf{U}_x + \dot{y}_j \mathbf{U}_y, \varphi_i) = (\gamma \mathbf{f} + \mathbf{P}_3, \varphi_i) + \mathbf{D} \mathbf{U}_j a(\varphi_j, \varphi_i) \quad (3.33)$$

for all $i, j = 1, \dots, N+1$. \mathbf{U}_x and \mathbf{U}_y are defined in relations (3.27) and (3.28) respectively. \dot{x}_j and \dot{y}_j are prescribed. Over each element, we assemble matrices $m_{i,j}$; $ux_{i,j}$; $uy_{i,j}$; $f_{i,j}$,

$p_{3i,j}$ and $k_{i,j}$, $i, j = 1, 2, 3$ called element matrices. All these element matrices are then assembled to give global matrices, leaving us with a time-dependent ordinary differential equation problem of the form

$$M \dot{\mathbf{U}} + \mathbf{D} K \mathbf{U} = (\gamma F + P)(\mathbf{U}) + (UX + UY) \mathbf{U}, \quad (3.34)$$

where M is the mass matrix, F and P result from the nonlinear terms (these depend on \mathbf{U}), K is the global stiffness matrix and UX and UY are the global matrices resulting from grid movement. If the domain is fixed in time, UX and UY are zero matrices. Solving (3.34) gives us an approximation to the classical solution \mathbf{u} .

3.3 Time-stepping

The discretisation of the time derivative and the linearisation of nonlinear terms are carried out simultaneously. The nonlinear terms can be written in matrix–vector–product form where the matrix depends on either U or both U and V (for specific details, see Madzvamuse, 2000). This form makes it possible to linearise the nonlinear terms by use of the Picard iteration method (Reddy, 1984). For example, the term U^2 , can be written as a product of $U^m U^{m+1}$ where U^m is the known solution calculated from the previous time $m \Delta t$. On a continuously moving grid this will be equivalent to calculating the successive solution U^{m+1} , where the previous solution U^m is evaluated on the new grid. The Picard iteration method is combined with the Implicit Backward Euler finite difference scheme to yield a robust and stable scheme. To solve the set of linear algebraic equations obtained, a Preconditioned Generalised Minimum Residual Method is used. Preconditioners such as ILU(0), ILUT, ILUTP, ILUK and MILU(0) can be used with the method (Saad, 1994, 1996). In all our simulations we employ ILU(0). The criterion for convergence to the inhomogeneous steady state and hence a stopping criterion is

$$\sqrt{\frac{\sum |\mathbf{U}^{m+1} - \mathbf{U}^m|^2}{\sum |\mathbf{U}^{m+1}|^2}} \leq \epsilon \quad (3.35)$$

with ϵ typically of the order 10^{-6} – 10^{-9} .

4 Transient solutions on regular and irregular growing domains

We investigate the role of domain growth on pattern selection and transition on regular and irregular growing domains. The assumption is that the evolution of the solutions of the model equations takes place on the same timescale as domain growth. In section 3, we pointed out that domain growth is prescribed. Biologically we assume that the nodal movement can be derived from experimental data. However, for illustrative purposes, we prescribe specific growth functions that continuously deform the domain.

One of the simplest ways to do this is to assume that the nodal movement can be written as a product of two functions, one that depends on the initial grid only and another that depends on time only. We can therefore define $x(t) = X r(t)$ and $y(t) = Y r(t)$, to

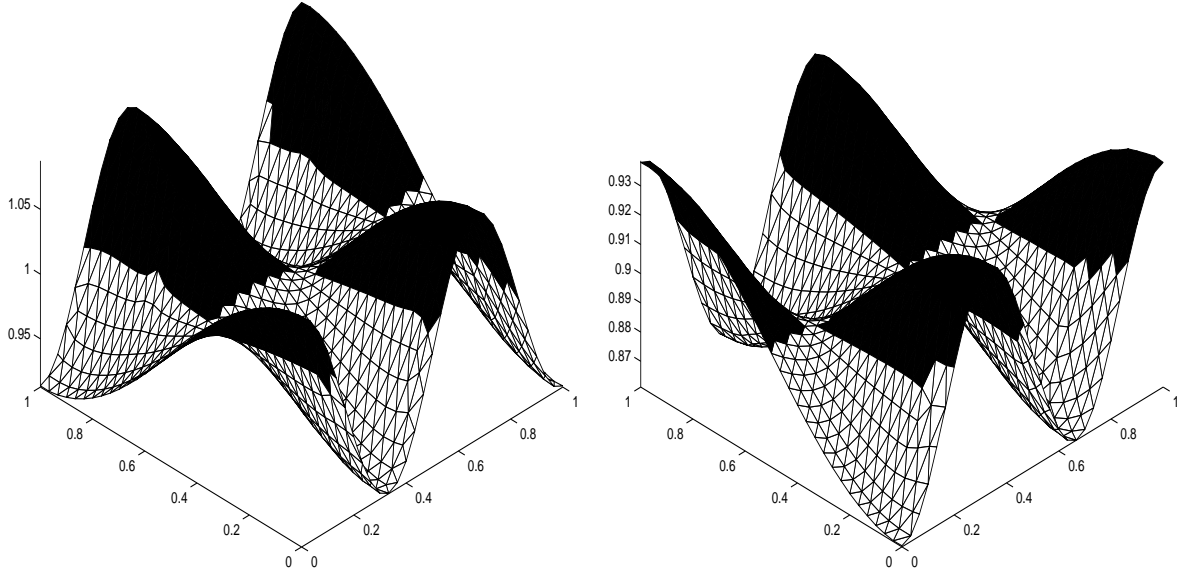


Figure 2: The solution surfaces of u and v illustrating the type of shading used.

represent the boundary grid movement where X and Y are the initial boundary grid coordinates of $x(0)$ and $y(0)$ respectively at time $t = 0$. The velocity of grid movement is given by $\dot{x}(t) = X \dot{r}(t)$ and $\dot{y}(t) = Y \dot{r}(t)$. The above is valid if the function $r(t)$ satisfies the property $r(0) = 1$ at time $t = 0$. For illustrative purposes we will choose an exponential function of the form $r(t) = e^{\sigma t}$, $t \geq 0$. One of the assumptions on domain growth is that it is slow and for this we require that σ be a small parameter. This form of domain growth has been used previously in the study of robust pattern formation under domain growth (Painter, 1997; Crampin, 1999). In their studies σ is assumed to be of the order 10^{-2} – 10^{-5} . For the sake of comparison with their work where possible, we assume that the parameter is of the same magnitude. Observe that the boundary continuously deforms. The new positions of the internal grid coordinates need to be calculated: here, we apply a spring analogy (Bloom, 2000) to calculate the internal mesh movement. The spring analogy is a common technique for deforming a mesh, it consists of replacing the mesh by fictitious springs. There are two types of springs, the vertex and the segment spring analogies. The vertex spring is used mainly to refine a particular mesh, while the segment spring is appropriate for deforming and moving a given mesh. This technique preserves the number of grid coordinates and the mesh connectivity which enables smooth evolution. The initial mesh and the boundary grid points are generated by a Delaunay mesh generator (Müller *et al.*, 1993).

In all our simulations the pattern transition on growing domains is independent of numerical parameters such as mesh size and time-step. By refining the mesh and time-step sizes, numerical solutions remain qualitatively similar with only small quantitative changes occurring. Numerical simulations have been carried out with different time-steps and different mesh sizes and the transition process was observed to be qualitatively unchanged. In all the simulations shown in this paper, the contour profiles of the inhomogeneous steady state solutions are plotted. This is mainly for biological interpretations.

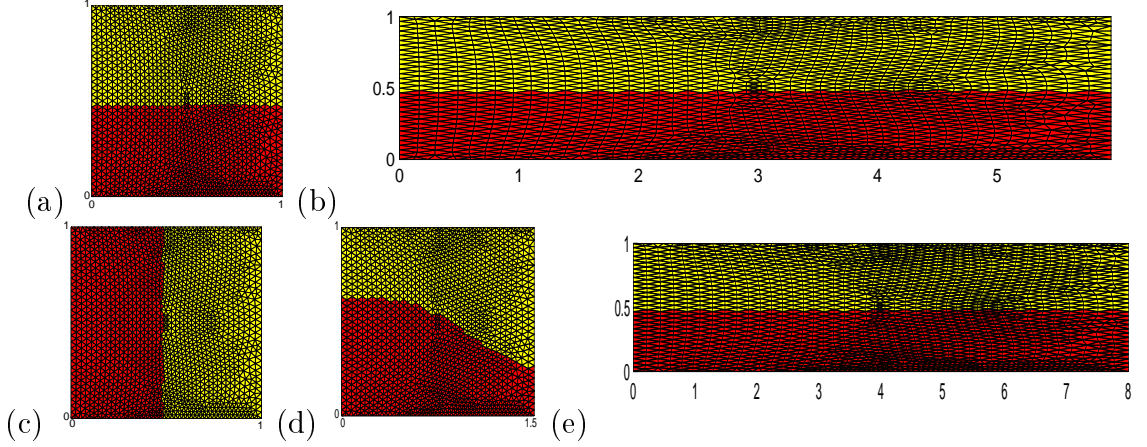


Figure 3: The domain $[0, 1] \times [0, 1]$ is grown exponentially to reach the final domain $[0, 6] \times [0, 1]$. The Schnakenberg model is solved with parameter values $a = 1.0$, $b = 0.9$, $\gamma = 29$ and $d = 10$. (a) and (b): A stripe is generated and simply elongates as the domain grows along the x -axis. (c)–(e): The unit square domain is grown exponentially to reach the final $[0, 8] \times [0, 1]$ domain. Initial conditions are chosen such that a stripe parallel to the y -axis is produced. The orientation of the pattern changes completely as the domain grows, a stripe emerges perpendicular the y -axis, recapturing the orientation in (b).

In biological context colour patterns are linked to cell differentiation. Assuming that colouration is determined by a constant threshold value in u (or v) concentration, u_s (or v_s) say, such that cells in the region where $u \geq u_s$ are black, while cells which experience a concentration $u < u_s$ are coloured white, these give rise to the shading illustrate in all the figures. The actual solution surfaces (u or v) are as depicted in Figure 2.

4.1 Transient solutions on regular domains: Schnakenberg kinetics

4.1.1 Stripe-to-stripe patterns

For illustrative purposes, we solve the Schnakenberg model equations with homogeneous Neumann boundary conditions applied to both u and v . Let us first consider square and rectangular domains. The simplest form of growth is when it occurs along one axis of the domain. This can be viewed as an extension of one-dimensional domain growth where values of x or of y are fixed as constants. A typical example of this growth is shown in Figure 3 (a) and (b). We let the initial unit square grow exponentially along the x -axis until it reaches the final domain, taken here to be $[0, 6] \times [0, 1]$. The numerically computed transient solutions of the model equations on a growing unit square in this example consist of an elongating stripe. From linear stability theory (Appendix A), the parameter values of γ and d are selected such that the $(1, 0)$ mode is isolated on a unit square. Linear stability theory predicts that $(0, 1)$ is always an excitable mode on the domain $[0, L] \times [0, 1]$ for any length L . The corresponding eigenfunction of the Laplacian with homogeneous Neumann boundary conditions on this domain can be shown to be given by $\cos \pi y$. Hence the

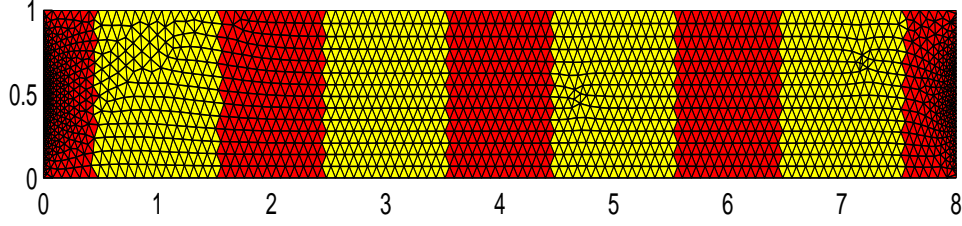


Figure 4: Numerically computed spatially inhomogeneous steady state solution on a fixed domain $[0, 8] \times [0, 1]$ with random initial conditions. This type of solution will never be observed on a growing unit square as shown in Figure 3 (a)–(e).

stripe pattern produced from the transient solutions is consistent with predictions from linear stability theory.

If, however we prescribe initial conditions which are biased towards the pattern generated by the eigenfunction $\cos \pi x$ on a unit square, we obtain the numerical solution illustrated in Figure 3 (c)–(e). As the unit square continues to grow exponentially along the x -axis, the transient solution changes orientation. The domain is grown until it reaches the size $[0, 8] \times [0, 1]$. In both simulations, the numerical solution of the model equations under this form of domain growth with these parameter values produces stripe patterns independent of initial conditions. This indicates that pattern selection under domain growth can be insensitive to initial conditions when these are small amplitude perturbations about the uniform steady state.

In order to highlight the crucial role of growth in pattern selection we illustrate in Figure 4 the result of solving the model equations on a fixed domain with homogeneous Neumann boundary conditions and a particular random initial condition but with exactly the same parameter values as in Figure 3. Instead of elongating horizontal stripes, vertical stripes are obtained. This solution would never be computed nor observed under the domain growth of Figure 3, and quite possibly under no form of dynamic domain elongation. Thus it is apparent that domain growth enhances the robustness of pattern selection.

4.1.2 Stripe-to-spot patterns

Let us consider now a different form of growth from the essentially one-dimensional form described previously. Suppose we let the unit square grow along the diagonal giving rise to successively larger square domains.

For illustrative purposes, we choose parameter values determined to isolate the $(1, 0)$ mode on a unit square. The transient solution of the model equations with these parameter values on a growing unit square are shown as the sequence of frames in Figure 5. As the domain grows a stripe pattern transforms into a spot pattern. This evolution process occurs through peak insertion, whereby a stripe evolves into a spot pattern. Further domain growth shows peak splitting from a single spot to four spots. This result has been observed before (Crampin *et al.*, 2002).

Hence we have observed in one simulation the insertion and splitting of peaks. As the

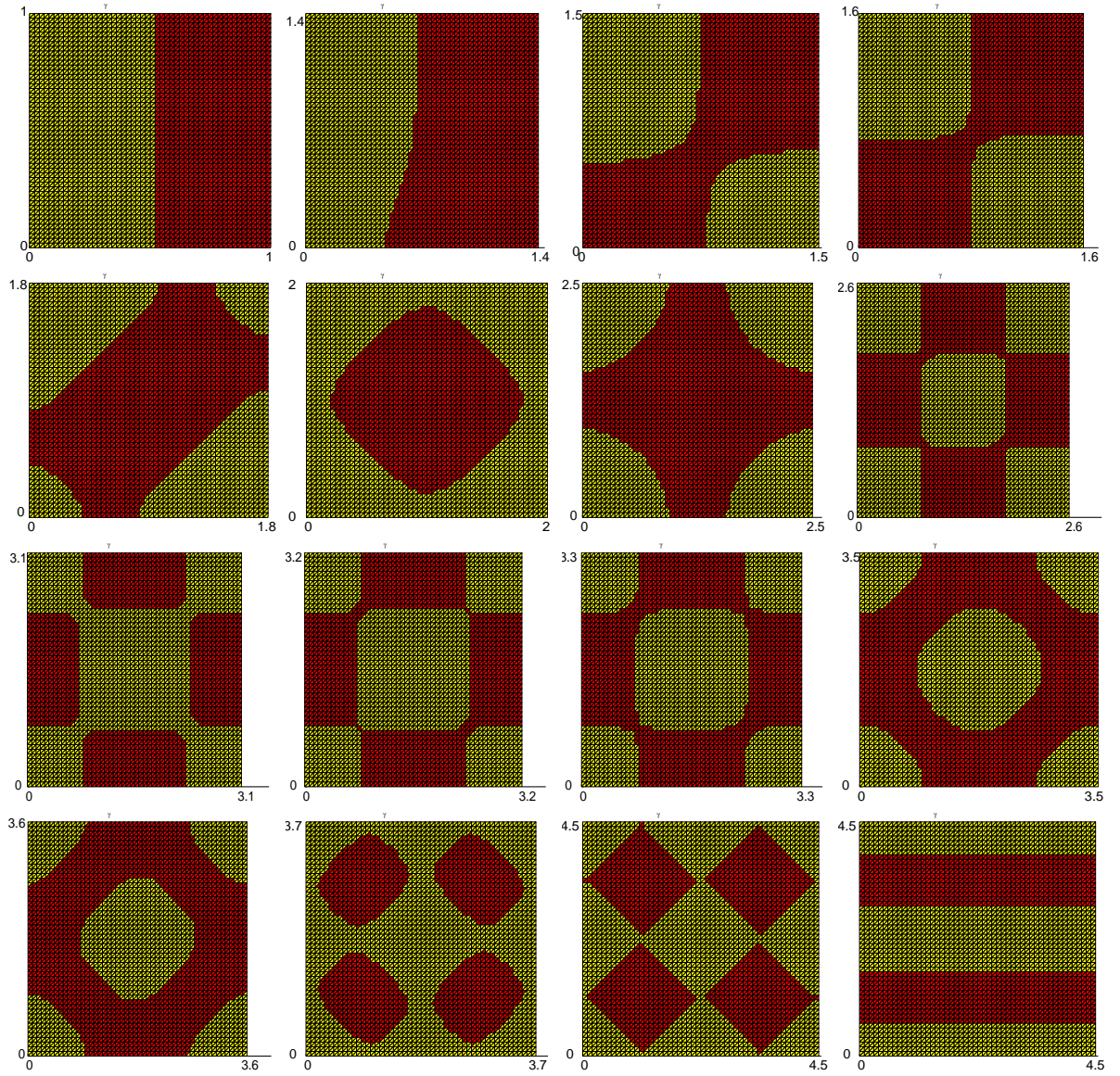


Figure 5: Transient patterns generated by the Schnakenberg model as the unit square is grown along the diagonal line $x = y$ at constant speed in the positive direction. The parameter values in the numerical computations are $a = 0.1$, $b = 0.9$, $d = 10$ and $\gamma = 10$. Stripes evolve to spots which in turn evolve into circular patterns as the domain grows. Further growth transforms these back into spots. However, when domain growth is stopped, the spatially inhomogeneous steady state solution computed to which the system converges is that of stripes. This type of solution will never be computed under this form of domain growth.

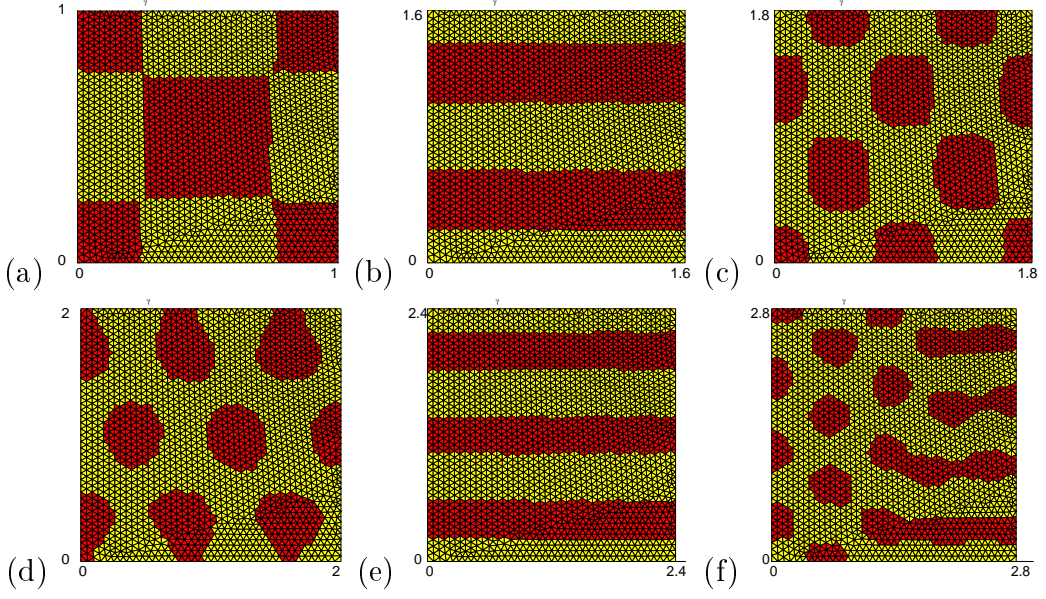


Figure 6: Transient solutions of the Schnakenberg model on the unit square growing along the diagonal $y = x$. The parameter values are chosen such that the $(2, 2)$ mode is isolated on a unit square. These are given as $a = 0.1$, $b = 0.9$, $d = 8.6676$ and $\gamma = 230.82$. The observed transient patterns are spots, stripes and spots alternating repeatedly as the domain grows.

evolution of four spots continues they merge to form oblique stripes due to peak insertion. When the growing domain reaches $[0, 3.5] \times [0, 3.5]$, a circular pattern is observed. On further growth, the domain passes through another transition point. Although the circular pattern is still more pronounced on the domain $[0, 3.6] \times [0, 3.6]$, we observe peak insertion as the domain grows. This gives rise to the formation of spots as the circular pattern breaks down. Spots are illustrated more clearly on the domains from $[0, 3.7] \times [0, 3.7]$ up to the domain $[0, 4.5] \times [0, 4.5]$. When the domain reaches the final domain size, taken here to be $[0, 4.5] \times [0, 4.5]$, the simulation converges to a spatially inhomogeneous steady state on this fixed domain. Surprisingly, stripes are produced in favour of spots. It appears therefore that growth stabilises spots over stripes. It certainly indicates that dynamic growth significantly affects patterning. However more detailed and extensive numerical experiments are required to confirm this. Different random initial conditions have been prescribed as small perturbations about the uniform steady state and we have observed qualitatively similar sequences, hence we conclude that pattern transition under domain growth is insensitive locally to initial data.

4.1.3 Spot-to-stripe-to-spot patterns

Figure 6 illustrates a pattern sequence in which spots and stripes are produced in an alternating fashion. Parameters are chosen such that linear theory predicts evolution to the $(2, 2)$ mode on the unit square. The corresponding eigenfunction is given by $\cos(2\pi x)\cos(2\pi y)$ with eigenvalue $k_{2,2} = 8\pi^2$. The pattern shown in Figure 6 (a) is

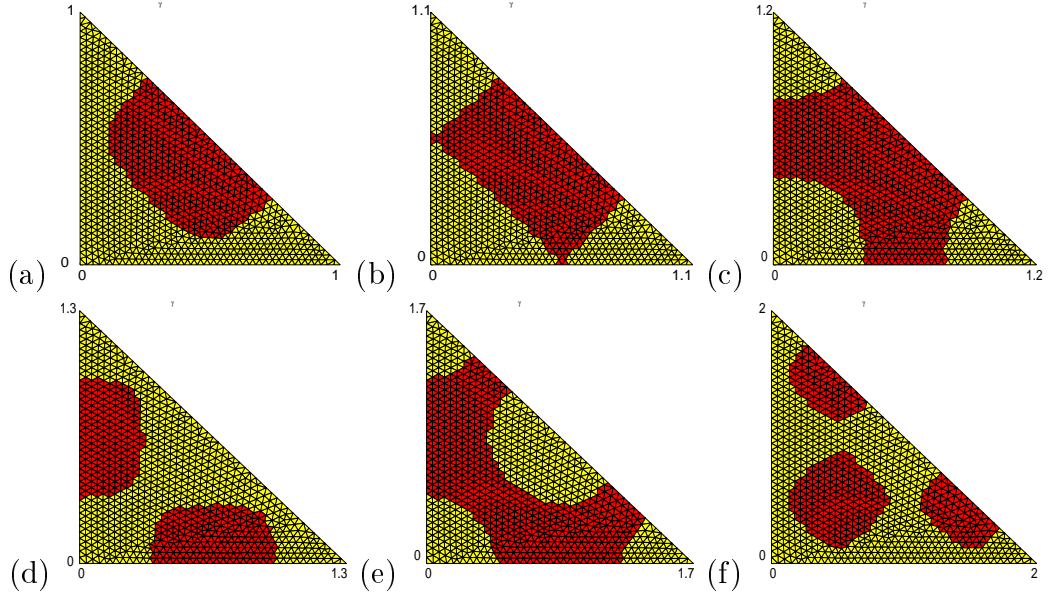


Figure 7: Patterns on a growing right-angled isosceles triangle for the Schnakenberg model with parameter values $a = 0.1$, $b = 0.9$, $d = 10$ and $\gamma = 114$. The initial triangle, with vertices $(0,0)$, $(1,0)$ and $(0,1)$ is grown exponentially along the diagonal $y = x$ until it reaches the triangle with vertices $(0,0)$, $(2,0)$ and $(0,2)$. These simulations show spots transforming into stripes and back to spots repeatedly.

obtained from the numerical solution of the model equations on a unit square and is consistent with this eigenfunction.

When the unit square is grown exponentially along the diagonal $y = x$ to reach the domain $[0, 1.6] \times [0, 1.6]$ it passes through a region where spots become inadmissible patterns. Instead of spots, stripes are formed (Figure 6 (b)). This process is independent of the initial conditions. We have carried out numerical tests with different initial conditions and with more refined grids and obtained the same results. On further growth, up to $[0, 1.8] \times [0, 1.8]$, the reverse takes place, stripes becoming inadmissible while spots are generated, as shown in Figure 6 (c). With further growth, this process is repeated (Figure 6 (d)–(f)). The pattern obtained in Figure 6 (e) compares qualitatively with the predictions from linear theory that the eigenfunction $\cos\left(\frac{6\pi}{2.4}y\right)$ of the Laplacian with zero-flux boundary conditions on this domain should grow. If domain growth stops, at say $[0, 2.8] \times [0, 2.8]$, and the simulations allowed to converge, the pattern produced is a mixture of spots and stripes.

So far we have investigated the role of domain growth by growing a unit square domain exponentially either along one of the axes to produce rectangular domains or along one of the diagonals producing square domains. We now extend this study to three different simple geometric domains, a right-angled isosceles triangle, an equilateral triangle and a hexagon.

4.1.4 Transient patterns on a right-angled isosceles triangle

Figure 7 illustrates the transient patterns on a growing right-angled isosceles triangle. We impose domain growth along the line of symmetry $y = x$. We proceed to solve the Schnakenberg model and for illustration purposes, we choose parameters determined from linear stability analysis such that the (2,0) mode is isolated on a unit square. Homogeneous Neumann boundary conditions are assumed with initial conditions given as random perturbations about the homogeneous steady state.

The numerical solution first produces a spot pattern as illustrated in Figure 7 (a). This compares well qualitatively with linear stability theory. The theory predicts that the eigenfunction of the Laplacian with homogeneous Neumann boundary conditions on this domain is given by $A \cos 2\pi x + B \cos 2\pi y$ with eigenvalue $k_{2,0}^2 = 4\pi^2$ and A, B constants. The pattern generated numerically is consistent with that predicted by linear stability theory. As the triangle grows exponentially to reach 1.1 units along both axes, small changes occur to the pattern (Figure 7 (b)), but in essence it compares qualitatively with the previous pattern shown in Figure 7 (a). However, on further growth of the triangle, the pattern starts to change substantially. For example, it can be seen that in Figure 7 (c) the pattern begins to split eventually to form two spots (Figure 7 (d)). Figure 7 (e) shows how these two spots evolve into stripes as the domain continues to grow. As the triangle continues to grow, spots are observed once more and if domain growth stops and the simulations allowed to converge, they produce the steady state illustrated in Figure 7 (f). Hence we see that pattern transitions produced on this growing right-angled triangle are qualitatively similar to those on the growing square domain. The transient solutions are insensitive to initial conditions.

4.1.5 Transient patterns on an equilateral triangle

We now consider patterns on an equilateral triangle given by the vertices $(0, -1)$, $(\sqrt{3}, 0)$ and $(0, 1)$ as shown in Figure 8 (a). We assume that domain growth is along the positive x -axis and in both the negative and positive directions of the y -axis. We compute transient solutions of the model equations with Neumann boundary conditions and random initial conditions. As in the previous section, the parameter values used in the computations are those determined from linear stability theory to isolate the mode (2, 0) on a unit square.

Figure 8 shows the patterns obtained from transient solutions of the model equations as the triangle is grown until it reaches the final equilateral triangle determined by the vertices $(0, -2)$, $(2\sqrt{3}, 0)$ and $(0, 2)$. As the triangle grows exponentially, spots are observed initially, increasing in number as the domain grows (Figure 8 (a)–(d)). It should be observed that in passing from Figure 8 (d) to (e) the spots merge together to form stripes. This becomes more pronounced as domain growth continues (Figure 8 (f)). In Figure 8 (g) we observe a combination of spots and stripes. The evolution of these patterns is independent of initial conditions for the given parameter values. When domain growth ceases and the simulations are allowed to converge they exhibit the inhomogeneous steady state pattern representing spots (Figure 8 (h)).

The transient solutions observed depict two properties, that is, either they are symmetrical with respect to a 120° rotation about the centre (Figure 8 (a)–(b)) or they are

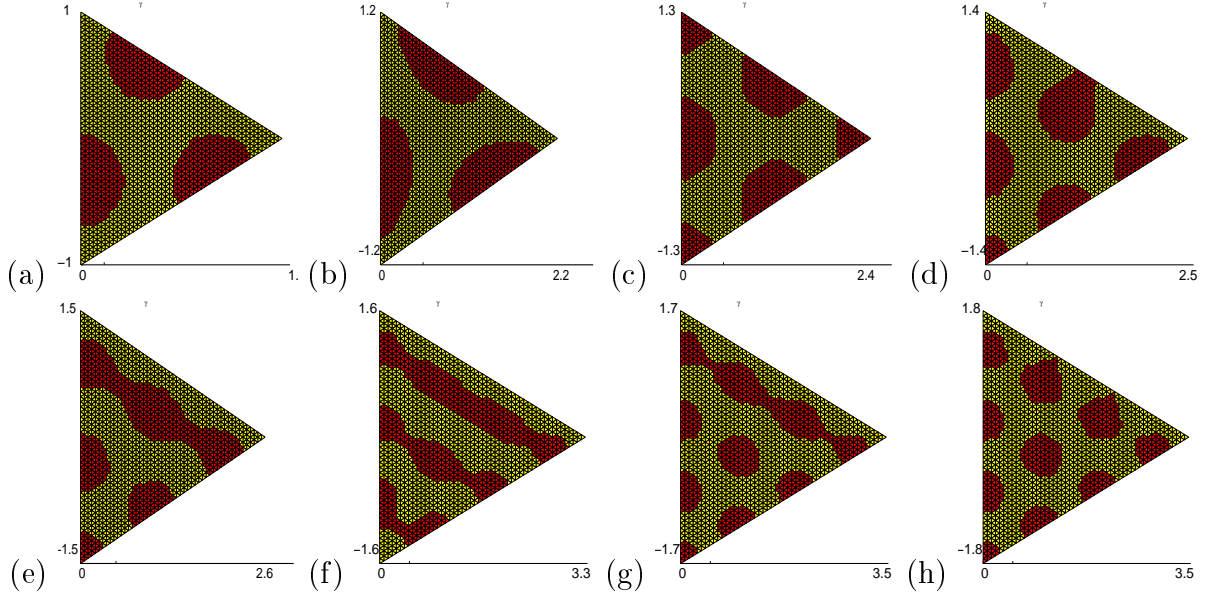


Figure 8: Transient solutions of the Schnakenberg model with zero-flux boundary conditions on a growing equilateral triangle. The parameter values are selected such that the $(2,0)$ mode is isolated on a unit square. As the domain grows, spots, stripes and spots are formed alternately.

symmetric about the altitude (Figure 8 (c)–(h)) passing through the lower vertex with x -coordinate zero.

4.1.6 Transient patterns on a hexagon

We now investigate the role of domain growth on a hexagon of unit side given by the vertices $(1, 0)$; $(\frac{1}{2}, \frac{\sqrt{3}}{2})$; $(-\frac{1}{2}, \frac{\sqrt{3}}{2})$; $(-1, 0)$; $(-\frac{1}{2}, -\frac{\sqrt{3}}{2})$ and $(\frac{1}{2}, -\frac{\sqrt{3}}{2})$. The hexagon is allowed to grow exponentially from its centre to three times its original size. Figure 9 shows the corresponding numerical solutions of the model system with homogeneous Neumann boundary conditions. The parameter values are unchanged from those used on the equilateral triangle.

Initially we observe stripes (Figure 9 (a)) evolving to spots as the domain grows as shown in Figure 9 (b). Then the spots evolve to stripes (Figure 9 (c) and (d)). A mixed mode solution then gives rise to circular patterns as illustrated in the sequence shown in Figure 9 (e)–(k). The circular patterns continue to evolve as the domain deforms continuously until it reaches its final size. On this fixed domain the spatially inhomogeneous steady state pattern obtained is that of stripes and spots combined (Figure 9 (l)). The sequence illustrated is independent of the initial conditions.

Although this sequence exhibits several features in common with our previous simulations above, a new pattern is observed, namely circular patterns. The appearance of such patterns seems to be due to the nature of the geometry. The circular patterns appear as transient solutions when stripes and spots occur at almost the same time but neither solution dominates due to domain growth. Such patterns have been observed in zebrafish

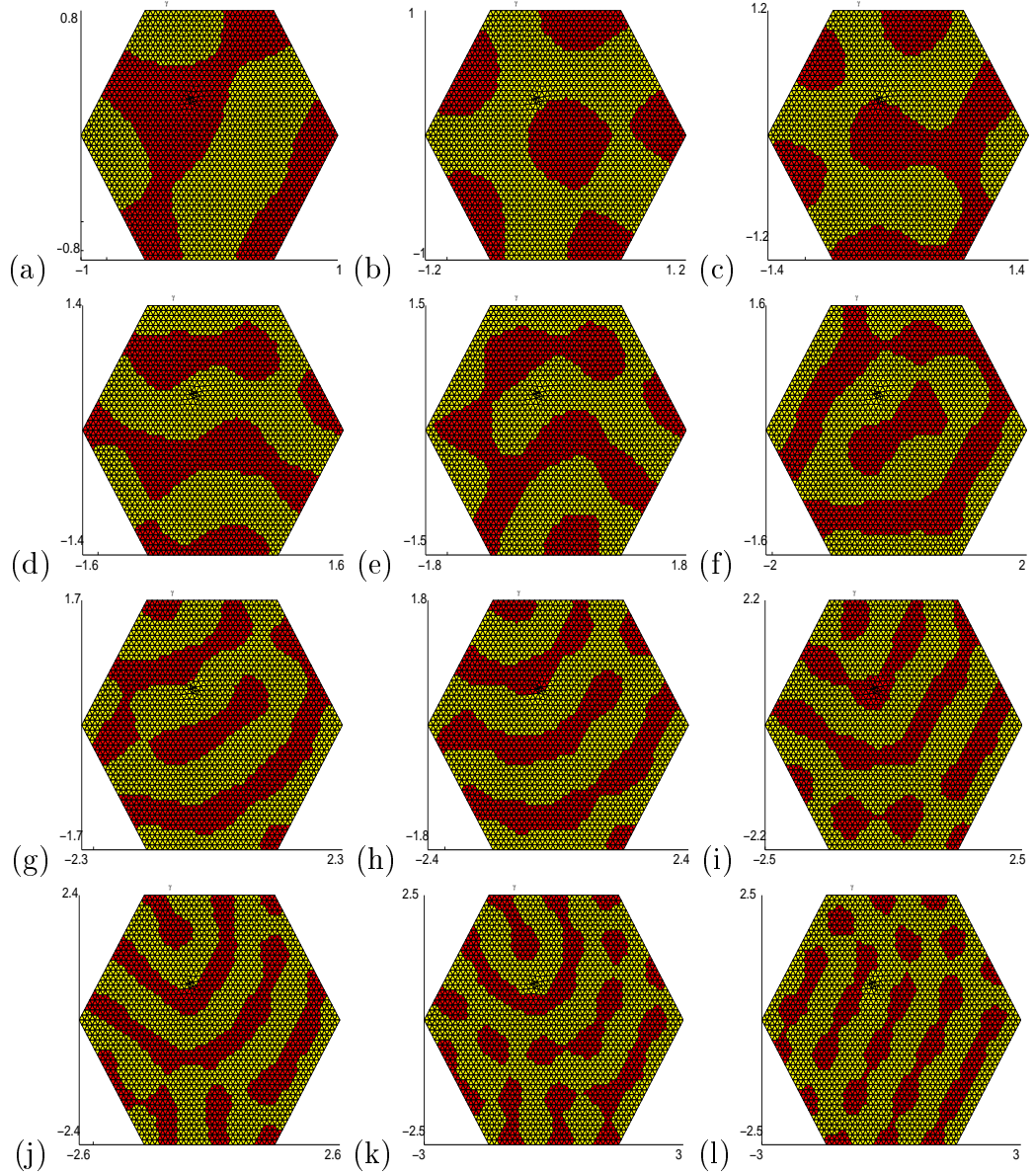


Figure 9: Typical numerically computed patterns on a growing hexagon for the Schnakenberg model with parameter values as in Figure 8. Stripe, spot and circular patterns are exhibited. Circular patterns become pronounced as the hexagon grows in size. As the domain reaches its maximum size, the system evolves to an inhomogeneous steady state solution consisting of stripes and spots.

(Painter *et al.*, 1999) and *Pomacanthus* (Kondo and Asai, 1995). This phenomenon could explain the emergence of circular patterns of pigmentation on fish which takes place as the fish grows in size. A combination of spots and stripes are observed when the zebrafish attains its maximum size, which compares qualitatively with the inhomogeneous steady state pattern computed on the final fixed domain. When the domain reaches its final size the numerical solution converges to a mixed pattern of stripes and spots (Figure 9 (l)). The evolution of the transient solutions on the growing domain is insensitive to the initial conditions. Therefore under domain growth the model is robust as the patterns generated are independent of the initial conditions, when these are small amplitude perturbations about the uniform steady state.

4.2 Transient solutions on irregular domains: Gierer-Meinhardt kinetics

The aim of this section is to illustrate the generality of our numerical technique in dealing with arbitrary simply connected domains. This work was motivated by the study of growth colour patterns in the butterfly wing *Papilio dardanus*. The biological background to the mathematical problem is well documented in the papers by Sekimura *et al.*, 1998, 1999, 2000; and in the book by Nijhout (1990). Our aim here is not to compute patterns typically observed in biological experiments but to illustrate the generality of our numerical method.

The problem here is, given a discrete sequence of the wing size and shape of the butterfly *Papilio dardanus* can we predict and calculate the evolving patterning process? Typically the discrete sequence is given by the scans at the following time intervals, 12, 36, 48, 60, 72 and 96 hours (Figure 10 and Table 1). Interpolation between the positions of the boundary nodes of the boundary shape is achieved with Cubic spline thus defining a continuously deforming domain. Once the boundary position of the continuously deforming boundary is located, the spring analogy is applied at each time step to define the internal mesh and hence to define the motion on the internal nodes.

We solve the Gierer-Meinhardt reaction kinetics with homogeneous Neumann boundary conditions for both u and v . We note that these are not realistic boundary conditions for the butterfly pattern (Sekimura *et al.*, 2000). Initial conditions are taken as random perturbations about a constant value. Figures 11 and 12 show the results of such computations. As the domain grows continuously transient patterns evolve from spots to circular patterns. The scale changes in Figures 11 and 12 are small compared to the rest of the previous figures. Therefore we plot the figures on the same scale $[-2, 2.6] \times [-2, 2]$ and this is not shown in the illustrated figures.

5 Conclusion and Discussion

The novel application of the moving grid finite element method to reaction-diffusion systems on a continuously deforming domain has opened new avenues in the study of pattern formation and transition in Biology. In particular, we have developed a freely available software package that can be used not only to investigate pattern formation, but also to predict pattern transition. All results reported in this paper are produced with this

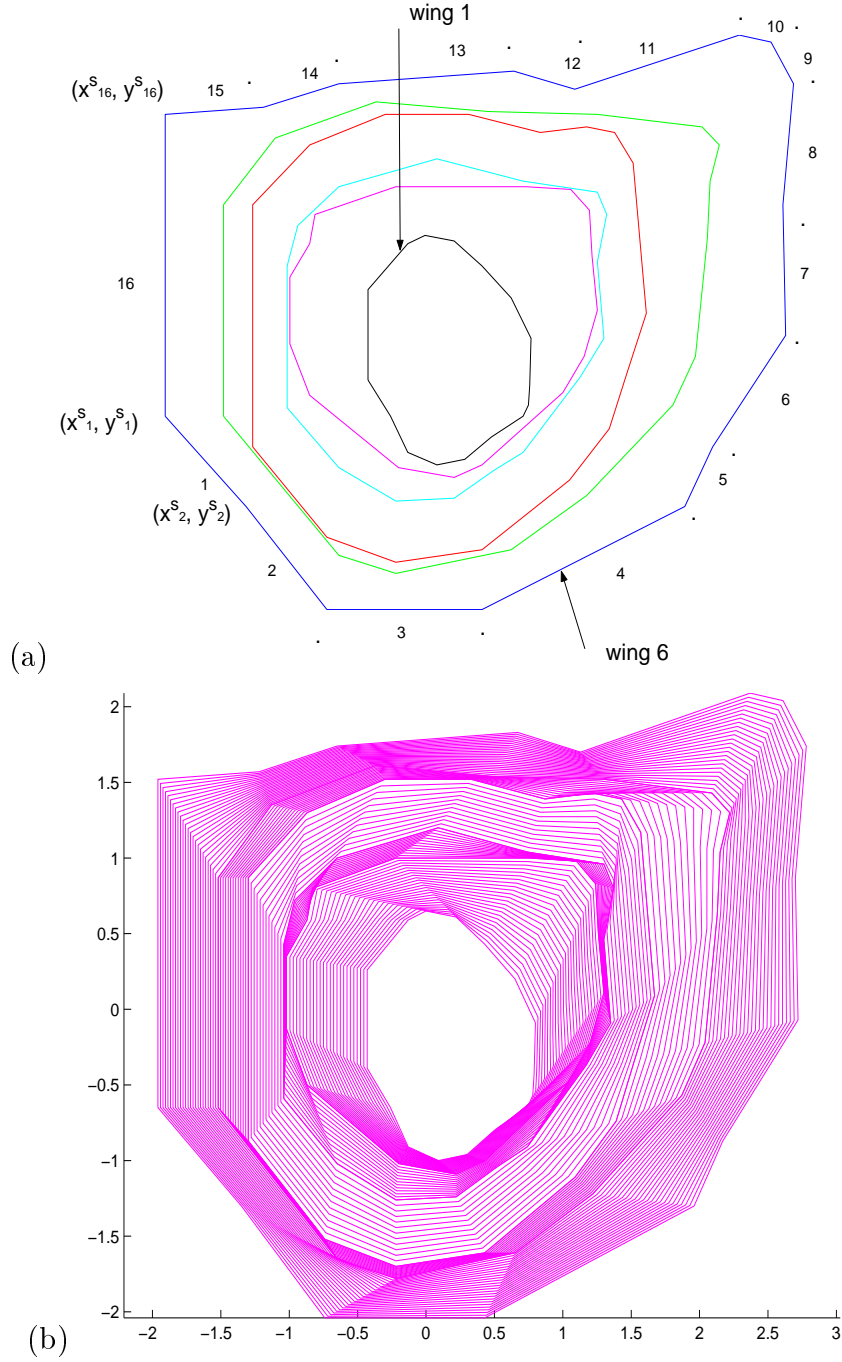


Figure 10: (a) The 16-sided polygonal approximation to the butterfly wing of *Papilio dardanus*. (b) A typical sequence of the polygons generated by the cubic spline interpolation at selected time intervals. The spring analogy is used to deform and move the mesh generated in wing 1 given successive locations of. All results reported in this paper are produced with this package and this can be downloaded from files as well as the the deforming boundary using cubic splines.

Time (s)	0.432×10^5	1.296×10^5	1.728×10^5	2.16×10^5	2.59×10^5	3.456×10^5
(x^{s_1}, y^{s_1})	(-0.43, -0.39)	(-1.02, -0.13)	(-1.04, -0.59)	(-1.3, -0.87)	(-1.52, -0.65)	(-1.96, -0.65)
(x^{s_2}, y^{s_2})	(-0.26, -0.65)	(-0.87, -0.5)	(-0.65, -1.02)	(-0.74, -1.52)	(-0.65, -1.65)	(-1.35, -1.3)
(x^{s_3}, y^{s_3})	(-0.13, -0.91)	(-0.2, -1.02)	(-0.22, -1.26)	(-0.22, -1.7)	(-0.22, -1.78)	(-0.74, -2.04)
(x^{s_4}, y^{s_4})	(0.09, -1.0)	(0.22, -1.09)	(0.22, -1.24)	(0.43, -1.61)	(0.65, -1.61)	(0.43, -2.04)
(x^{s_5}, y^{s_5})	(0.3, -0.96)	(0.43, -1.0)	(0.52, -1.04)	(1.09, -1.11)	(1.22, -1.22)	(1.96, -1.3)
(x^{s_6}, y^{s_6})	(0.5, -0.8)	(1.04, -0.48)	(0.74, -0.91)	(1.39, -0.74)	(1.87, -0.57)	(2.17, -0.87)
(x^{s_7}, y^{s_7})	(0.74, -0.65)	(1.2, -0.22)	(1.17, -0.37)	(1.52, -0.35)	(2.04, -0.22)	(2.72, -0.07)
(x^{s_8}, y^{s_8})	(0.78, -0.57)	(1.3, 0.11)	(1.35, -0.09)	(1.67, 0.09)	(2.13, 0.63)	(2.7, 0.87)
(x^{s_9}, y^{s_9})	(0.79, -0.43)	(1.26, 0.5)	(1.3, 0.46)	(1.57, 1.17)	(2.15, 1.04)	(2.78, 1.74)
$(x^{s_{10}}, y^{s_{10}})$	(0.8, -0.09)	(1.24, 0.83)	(1.37, 0.8)	(1.43, 1.39)	(2.22, 1.3)	(2.61, 2.04)
$(x^{s_{11}}, y^{s_{11}})$	(0.65, 0.2)	(1.1, 0.98)	(1.3, 0.96)	(1.22, 1.43)	(2.09, 1.43)	(2.37, 2.09)
$(x^{s_{12}}, y^{s_{12}})$	(0.43, 0.43)	(0.76, 1.0)	(0.74, 1.04)	(0.87, 1.39)	(1.30, 1.52)	(1.13, 1.7)
$(x^{s_{13}}, y^{s_{13}})$	(0.22, 0.61)	(-0.22, 1.0)	(0.09, 1.2)	(0.33, 1.52)	(0.4, 1.54)	(0.67, 1.83)
$(x^{s_{14}}, y^{s_{14}})$	(0.0, 0.65)	(-0.83, 0.8)	(-0.65, 1.0)	(-0.3, 1.52)	(-0.37, 1.61)	(-0.65, 1.74)
$(x^{s_{15}}, y^{s_{15}})$	(-0.13, 0.59)	(-0.87, 0.59)	(-0.96, 0.72)	(-0.87, 1.3)	(-1.13, 1.35)	(-1.22, 1.57)
$(x^{s_{16}}, y^{s_{16}})$	(-0.43, 0.26)	(-1.02, 0.35)	(-1.04, 0.43)	(-1.3, 0.87)	(-1.52, 0.87)	(-1.96, 1.52)

Table 1: The boundary coordinates of the 16-sided polygonal domain of the six wings in Figure 10. Here s_k represents the location of the (x, y) end points on each segment of the polygon.

package and this can be downloaded from:

<http://users.comlab.ox.ac.uk/anotida.madzvamuse/software/>.

This technique has been applied to the study of colour pattern formation of the butterfly wing *Papilio dardanus* (Sekimura *et al.*, 2000; Madzvamuse *et al.* 2002), and growth patterns in bivalve ligaments (Thomas *et al.*, 2000; Madzvamuse *et al.*, 2002).

We have observed that stripes can evolve into stripes, spots into spots and sometimes stripes evolve into spots which in turn involve into circular patterns. The emergence of such exotic patterns is due to the complexity of the domain. Domain growth appears to enhance robustness in pattern selection and transition: lack of robustness has been one of the main criticisms of the Turing theory of pattern formation on fixed domains.

The generality of our numerical method allows us to carry out further investigative real studies into pattern transition in biological problems. Currently we are investigating growth patterns of the butterfly wing *Papilio dardanus* and of the zebrafish.

Acknowledgements: This work (AM and AJW) was supported by a grant from EPSRC Life Sciences Initiative (GR/R03914). PKM was partly supported by a Royal Society Leverhulm Trust Senior Fellowship.

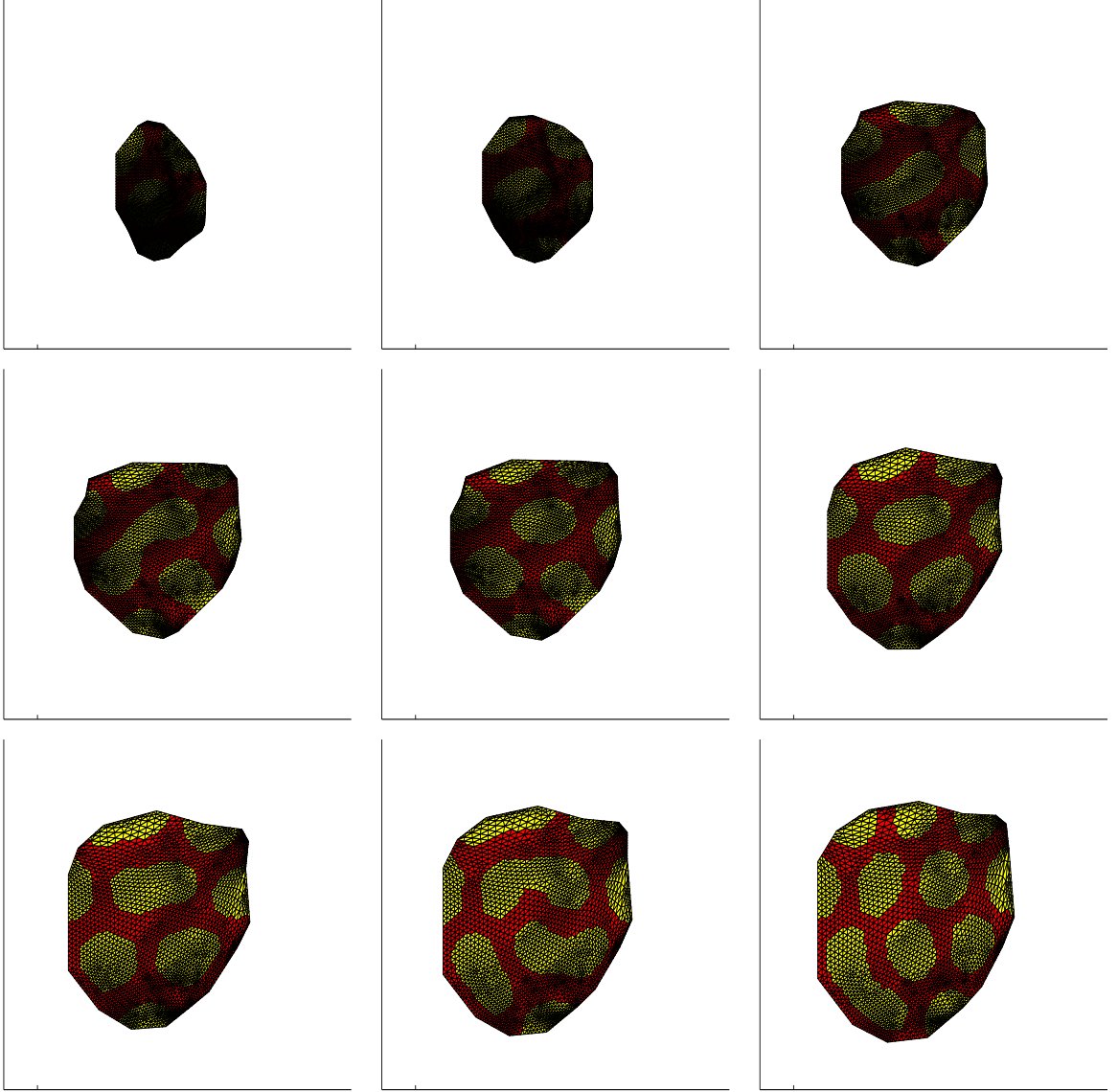


Figure 11: Transient patterns of the solution u corresponding to the Gierer-Meinhardt reaction model with parameter values $a = 0.1$, $b = 1.0$, $K = 0.5$, $d = 70.8473$ and $\gamma = 619.45$. Spot patterns continue to evolve with domain growth.

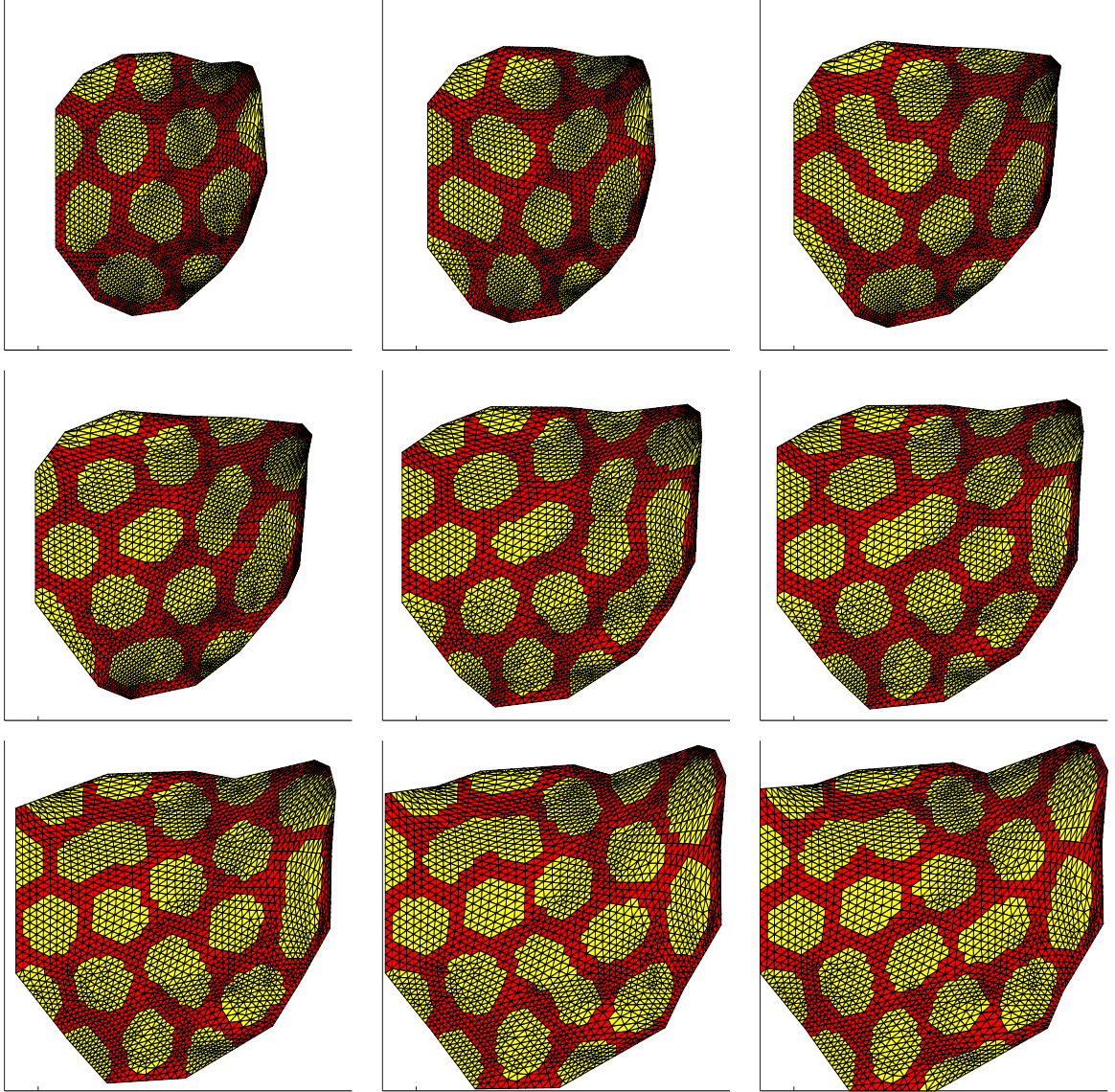


Figure 12: Figure 11 continued. As the domain continuously deforms, a combination of stripes and spots are exhibited on the same domain.

Appendix A: Linear Analysis

Standard linear stability analysis shows that diffusion-driven instability of a steady state of the systems (2.3)–(2.9) occurs if the following conditions hold (see, for example, the books by Edelstein-Keshet, 1988; Murray, 1993)

$$f_u + g_v < 0, \quad (5.1)$$

$$f_u g_v - f_v g_u > 0, \quad (5.2)$$

$$d f_u + g_v > 0, \quad (5.3)$$

$$(d f_u + g_v)^2 - 4 d (f_u g_v - f_v g_u) > 0, \quad (5.4)$$

where the partial derivatives are evaluated at the steady state. The inequalities (5.1)–(5.4) define a domain of parameter space, known as the Turing space, wherein the uniform steady state is unstable to random small perturbations.

Under these conditions, spatial disturbances with wavenumbers $k \in (k_-, k_+)$ will initially grow, where

$$k_{\pm}^2 = \gamma \frac{(d f_u + g_v) \pm \sqrt{(d f_u + g_v)^2 - 4 d (f_u g_v - f_v g_u)}}{2 d} \quad (5.5)$$

are the roots of the function on the left-hand side of (5.4). In the case we are interested in, namely, the unit square with zero flux boundary conditions, a further restriction on k is that it must take discrete values $\pi \sqrt{m^2 + n^2}$, corresponding to the spatial mode $\cos m \pi x \cos n \pi y$ denoted by (m, n) .

For diffusion-driven instability to occur we require that the Turing conditions (5.1)–(5.4) are satisfied and if we wish to isolate a certain mode, say (m, n) , then

$$k_{max}^2 \leq k_-^2 < k_{m,n}^2 = \pi^2(m^2 + n^2) < k_+^2 \leq k_{min}^2 \quad (5.6)$$

where

$$k_{max}^2 = \max\{\forall k_{p,q}^2 : k_{p,q}^2 < k_{m,n}^2 \text{ for some } p, q\}, \quad (5.7)$$

$$k_{min}^2 = \min\{\forall k_{p,q}^2 : k_{p,q}^2 > k_{m,n}^2 \text{ for some } p, q\}. \quad (5.8)$$

We impose the lower k_{max}^2 and upper k_{min}^2 bounds on k_-^2 and k_+^2 respectively so that $k_{m,n}^2$ will be the only eigenvalue with a positive real part. We wish to isolate a certain mode, that is, we want linear stability analysis to predict that the uniform steady state goes unstable only to spatial perturbations $\cos m \pi x \cos n \pi y$ with a particular (m, n) . Table 2 shows the parameter values d and γ for some fixed parameter values:

1. Gierer-Meinhardt model: $a = 0.1$, $b = 1.0$, $k = 0.5$;
2. Thomas model: $a = 150$, $b = 100$, $K = 0.05$, $\alpha = 1.5$ $\rho = 13$;
3. Schnakenberg model: $a = 0.1$ and $b = 0.9$.

Mode	Gierer–Meinhardt		Thomas		Schnakenberg	
(m,n)	d	γ	d	γ	d	γ
(1,0)	520.1573	67	427.0152	44	10	29
(1,1)	105.1573	168.8	39.0152	79	11.5776	70.6
(2,0)	84.1573	238.26	54.0152	122	10	114
(2,1)	77.6473	411.42	29.0152	170	9.1676	176.72
(2,2)	75.1573	483.43	30.9152	252	8.6676	230.82
(3,0)	70.8473	619.45	36.0152	269	8.6176	265.22
(3,1)	72.1573	756.23	27.5152	320	8.6676	329.20
(3,2)	73.1573	901.38	28.4152	402	8.8676	379.21
(3,3)	70.5573	1266.99	28.5152	553	8.6076	535.09
(4,0)	71.1573	1033.51	31.5152	473	8.6676	435.99
(4,1)	70.3573	1164.86	27.0252	506	8.5876	492.28
(4,2)	71.1573	1519.87	27.0252	596	8.7176	625.35
(4,3)	71.1573	1580.66	27.0252	745	8.6676	666.82
(4,4)	73.1473	2167	27.0252	953	8.6076	909.66

Table 2: Values for d and γ under which a particular mode is isolated on a unit square domain for the Gierer–Meinhardt, Thomas and Schnakenberg models.

Appendix B: Cubic spline interpolation

The basic idea of a cubic spline interpolation is that given a tabulated function, $x_i = x_i(t_i)$, $y_i = y_i(t_i)$, $i = 1, \dots, n$, determine the intermediate values of (x, y) of the function say between frame 1 and 2, that is at time 12 and 18 hours, every 15 seconds. n is the number of frames. For illustrative purposes, let us consider the time interval t_i and t_{i+1} , $i = 1, \dots, n - 1$. The aim is to obtain an interpolation formula that is smooth in the first derivative and continuous in the second derivative, both within an interval and at its boundaries. The interpolation can be shown to be of the form

$$(x, y) = C_0(x_j, y_j) + C_1(x_{j+1}, y_{j+1}) + C_2(x_j'', y_j'') + C_3(x_{j+1}'', y_{j+1}'') \quad (5.9)$$

with $j = 1, \dots, nbry$, $nbry$ is the number of boundary grid coordinates. $''$ denotes the second derivative with respect to time, and $C_0 = \frac{t_{j+1}-t}{t_{j+1}-t_j}$, $C_1 = 1 - C_0 = \frac{t-t_j}{t_{j+1}-t_j}$, $C_2 = \frac{1}{6} (C_0^3 - C_0) (t_{j+1} - t_j)^2$, $C_3 = \frac{1}{6} (C_0^3 - C_0) (t_{j+1} - t_j)^2$. Now assuming continuity of the first derivative across the boundary between any two intervals, gives rise to the system of equations

$$\begin{aligned} & \frac{t_j - t_{j-1}}{6} (x_{j-1}'', y_{j-1}'') + \frac{t_{j+1} - t_{j-1}}{3} (x_j'', y_j'') + \frac{t_{j+1} - t_j}{6} (x_{j+1}'', y_{j+1}'') \\ &= \frac{(x_{j+1}, y_{j+1}) - (x_j, y_j)}{t_{j+1} - t_j} - \frac{(x_j, y_j) - (x_{j-1}, y_{j-1})}{t_j - t_{j-1}}. \end{aligned} \quad (5.10)$$

In our case uniqueness is guaranteed by setting both the second derivatives of (x, y) at the end points equal to zero, giving the so-called *natural cubic spline*. Equation (5.10) is

tridiagonal, which is a huge practical advantage. Therefore the system of equations are solved in $O(N)$ operations by the tridiagonal algorithm.

Once the (\mathbf{X}, \mathbf{Y}) boundary coordinates are obtained through the cubic spline interpolation, we apply the spring analogy to calculate and move the new interior coordinates from the old coordinates.

Mesh movement using the spring analogy

The spring analogy is a common technique of deforming a mesh (Blom, 2000). It consists of replacing the mesh by fictitious springs. There are two types of springs, the vertex and the segment spring analogies. The vertex spring is used mainly to refine a particular mesh, while the segment spring is appropriate for deforming and moving a given mesh. In both cases, the segments are considered as springs. The springs are linear and Hookes' law is applied to determine the displacements of the nodes. For the segment springs, the equilibrium lengths of the springs are equal to the initial lengths of the segments. The force at each node i , say, is determined by

$$\mathbf{F}_i = \sum_{j=1}^{n_i} \alpha_{ij} (\delta_j - \delta_i). \quad (5.11)$$

Here, δ_i is the displacement of node i , n_i is the total number of nodes surrounding node i . α_{ij} is the spring stiffness which according to Batina (1990), is given by $\alpha_{ij} = \frac{1}{\sqrt{(x_i - x_j)^2 + (y_i - y_j)^2}}$. At static equilibrium, \mathbf{F}_i is zero, and applying Dirichlet boundary conditions, we obtain a system of linear algebraic equations whose unknowns are new displacements. The nodal displacement are therefore calculated as $\mathbf{x}_i^{\text{new}} = \mathbf{x}_i^{\text{old}} + \delta_i^{\text{final}}$.

Observe that the system,

$$\mathbf{O}_i = \sum_{j=1}^{n_i} \alpha_{ij} (\delta_j - \delta_i) \quad (5.12)$$

is symmetric and positive definite. The resultant matrix on the left-hand side for the unknown displacements is an M-matrix. When a boundary is moved or deformed, the boundary nodal positions are strongly imposed by Dirichlet boundary conditions. The system is solved by a preconditioned Conjugate Gradient method where the preconditioner is determined by an Incomplete Cholesky Factorisation (Saad, 1994).

References

- [1] ADAMS R.A. *Sobolev Spaces*. Academic Press, New York. (1975).
- [2] ARAGÓN J.L.; VAREA C.; BARRIO R.A. AND MAINI P.K. Spatial patterning in modified Turing systems: Application to pigmentation patterns on Marine fish. *Forma*, pp. 213-221, **13**, (1998).
- [3] ARAGÓN J.L.; TORRES M.; GIL D.; BARRIO R.A. AND MAINI P.K. Turing patterns with pentagonal symmetry. *Physical Review E*. pp. 1-9, **65**, (2002).
- [4] BAINES M. J. *Moving finite elements, Monographs on Numerical Analysis*. Clarendon Press, (1994).
- [5] BAINES M.J. AND WATHEN A.J.,. Moving finite element methods for evolutionary problems. *I. Theory. J. of Comp. Phys.* pp. 245-269, **79**, (1988).
- [6] BALKAREI Y.I.; GRIGOR'YANTS A.V.; RHZANOV Y.A. AND ELINSON M.I. Regenerative oscillations, spatial-temporal single pulses and static inhomogeneous structures in optically bistable semiconductors. *Opt. Commun* pp. 161-166, **66**, (1988).
- [7] BARRIO R.A.; VAREA C.; ARAGÓN J.L. AND MAINI P.K. A two-dimensional numerical study of spatial pattern formation in interacting systems. *Bull. Math. Biol.* pp. 483-505, **61**, (1999).
- [8] BARRIO R.A.; MAINI P.K.; ARAGÓN J.L. AND TORRES, M. Size-dependent symmetry breaking in models for morphogenesis. *Physica D*. pp. 1-12, **2920**, (2002).
- [9] BATIMA J. T. Unsteady Euler airfoil solutions using unstructured dynamic meshes. *AIAA Journal*. **28**(8), pp. 1381-1388, (1990).
- [10] BLOM. J. F.. Considerations of the spring analogy. *Int. J. Numer. Meth. Fluids*. **12**, pp. 647-668, (2000).
- [11] BRENNER S.C. AND SCOTT, L.R. *The Mathematical Theory of Finite Element Methods*. Springer. (1994).
- [12] CRAMPIN E.J.; GAFFNEY E.A. AND MAINI P.K. Reaction and diffusion on growing domains: Scenarios for robust pattern formation. *Bull. Math. Biol.* pp. 1093-1120, **61**, (2002).
- [13] EDELSTEIN-KESHET L. *Mathematical Models in Biology*. Random House, New York. (1988).
- [14] FIFE P. *Mathematical Aspects of Reacting and Diffusing Systems. Lecture Notes in Biomathematics*. Springer-Verlag. (1979).
- [15] GRAY P. AND SCOTT S.K. Autocatalytic reactions in the isothermal, continuous stirred tank reactor: isolas and other forms of multistability. *Chem. Eng. Sci.* pp. 29-43, **38** (1), (1983).

- [16] GRAY P. AND SCOTT S.K. Autocatalytic reactions in the isothermal, continuous stirred tank reactor: Oscillations and the instabilities in the system $A + 2B \longrightarrow 3B$, $B \longrightarrow C$,. *Chem. Eng. Sci.* pp. 1087-1097, **39** (6), (1984).
- [17] GIERER A. AND MEINHARDT H. A theory of biological pattern formation. *Kybernetik* **12**, pp. 30-39, (1972).
- [18] GRINDROD P. *The Theory and Applications of Reaction-Diffusion Equations Pattern Waves*. Clarendon Press. Oxford. 2nd Edition. (1996).
- [19] JIMACK P.K. AND WATHEN A.J. Temporal derivatives in the finite element method on continuously deforming grids. *SIAM J. Numer. Anal.* pp. 990-1003, **28** (4), (1991).
- [20] JOHNSON C. *Numerical Solution of Partial Differential Equations by the Finite Element Method*. Cambridge University Press. (1987).
- [21] KONDO S. AND ASAI R. A reaction-diffusion wave on the skin of the marine angelfish *Pomacanthus*. *Nature* pp. 765-768, **376**, (1995).
- [22] KRINSKY V.I. *Self-organisation, Auto-Waves and Structures Far From Equilibrium*. Springer, Berlin. (1984).
- [23] MADZVAMUSE A. *A numerical approach to the study of spatial pattern formation. D Phil Thesis*. University of Oxford. (2000).
- [24] MADZVAMUSE A.; MAINI P.K.; WATHEN A.J.; AND SEKIMURA T. A predictive model for color pattern formation in the butterfly wing of *Papilio dardanus*. *Hiroshima Math. J.* pp. 325-336, **32**, (2002).
- [25] MADZVAMUSE A.; THOMAS R.D.K.; MAINI P.K. AND WATHEN A.J. A numerical approach to the study of spatial pattern formation in the Ligaments of Arcoid Bivalves. *Bull. Math. Bio.* pp. 501-530, **64**, (2002).
- [26] MAINI P.K. AND SOLURSH M. Cellular mechanisms of pattern formation in the development of limb. *Int. Rev. Cytology*. pp. 91-133, **129**, (1991).
- [27] MEINHARDT H. *The Algorithmic Beauty of Sea Shells*. Heidelberg, New York, Springer-Verlag (1995).
- [28] MILLER K. Moving finite elements. Part I. *SIAM J. of Numerical Anal.* pp. 1019-1032, **18**, (1981).
- [29] MILLER K. Moving finite elements. Part II. *SIAM J. of Numerical Anal.* pp. 1019-1032, **18**, (1981).
- [30] MÜLLER J.D.; ROE P.L. AND DECONINCK H. A frontal approach for internal node generation for Delaunay triangulation. *Int. J. of Num. Meth. in Fluids*. **17**(3), pp. 241-256, (1993).

- [31] MURRAY J.D. On pattern formation mechanisms for lepidopteran wing patterns and mammalian coat markings. *Phil. Trans. R. Soc. Lond.* pp. 473-496, **B (295)**, (1981).
- [32] MURRAY J.D. *Mathematical Biology*. Heidelberg NY, Springer-Verlag. (1993).
- [33] NIJHOUT H.F. A comprehensive model for colour pattern formation in butterflies. *Proc. R. Soc. Lond.* pp. 81-113, **B (239)**, (1990).
- [34] NOZAKURA T. AND IKEUCHI S. Formation of dissipative structures in galaxies. *Astrophys. J.* pp. 40-52, **279**, (1984).
- [35] PAINTER K.J. *Chemotaxis as a Mechanism for Morphogenesis. D Phil Thesis*. University of Oxford. (1997).
- [36] PAINTER K.J.; MAINI P.K. AND OTHMER H.G. Stripe formation in juvenile *Pomacanthus* explained by a generalised Turing mechanism with chemotaxis. *Proc. Nat. Acad. Sci. USA.* pp. 5549-5554, **96**, (1999).
- [37] REDDY T.N., *An Introduction to the Finite Element Method*. McGraw-Hill. (1984).
- [38] SAAD Y. SPARSEKIT, *a basic tool kit for sparse matrix computations*. <http://www-users.cs.umn.edu/saad/> (1994).
- [39] SAAD Y. *Iterative Methods for Sparse Linear Systems*. PWS Publishing Co. (1996).
- [40] SCHNAKENBERG J. Simple chemical reaction systems with limit cycle behavior. *J. Theor. Biol.* pp. 389-400, **81**, (1979).
- [41] SEGEL L.A. AND JACKSON J.L. Dissipative structure: An explanation and an ecological example. *J. theor. Biol.* pp. 545-559, **37**, (1972).
- [42] SEKIMURA T.; MAINI P.K.; NARDI J.B.; ZHU M. AND MURRAY J.D. Pattern formation in lepidopteran wings. *Comments Theor. Biol.* **5: No.2-4**, pp. 69-87, (1998).
- [43] SEKIMURA T.; ZHU M.; COOK J.; MAINI P.K. AND MURRAY J.D. Pattern formation of scale cells in lepidoptera by differential origin-dependent cell adhesion. *Bull. Math. Biol.* **61**, pp. 807-827, (1999).
- [44] SEKIMURA T.; MADZVAMUSE A.; WATHEN A.J. AND MAINI P.K., A model for colour pattern formation in the butterfly wing of *Papilio dardanus*. *Proc. Roy. Soc. London.* pp. 851-859, **B(267)**, (2000).
- [45] THOMAS D. Artificial enzyme membrane, transport, memory and oscillatory phenomena. *Analysis and Control of Immobilised Enzyme Systems* Edited by D. Thomas and J.-P. Kervenez: Berlin Heidelberg, New York: Springer Verlag. pp. 115-150, (1975).

- [46] THOMAS R.D.K.; MADZVAMUSE A.; MAINI P.K. AND WATHEN A.J. Growth patterns of noetiid ligaments: implications of developmental models for the origin of an evolutionary novelty among arcoid bivalves. *The Evolutionary Biology of the Bivalvia* Edited by E. M. Harper, J.D. Taylor and J. A. Crame. Geological Society Special Publication. pp. 289-279, **177**, (2000).
- [47] TURING A.M. The chemical basis of morphogenesis. *Phil. Trans. Roy. Soc. Lond.* pp. 37-72, **B (237)**, (1952).
- [48] WHITE D.B. The planforms and onset of convection with a temperature dependent viscosity. *J. Fluid Mech.* pp. 247–286, **191**, (1988).